Chemistry Faculty Research & Creative Works   Chemistry

01 Aug 2014

Phosphorous Acid Route Synthesis of Iron Tavorite Phases, LiFePO$_4$(OH)$_x$F$_{1-x}$ [0 ≤ X ≤ 1] and Comparative Study of Their Electrochemical Activities

Hooman Yaghoobnejad Asl

Amitava Choudhury
Missouri University of Science and Technology, choudhurya@mst.edu

Recommended Citation

Phosphorous acid route synthesis of iron tavorite phases, LiFePO$_4$(OH)$_x$F$_{1-x}$ [0 ≤ x ≤ 1] and comparative study of their electrochemical activities†

Hooman Yaghoobnejad Asl and Amitava Choudhury*

New synthesis routes were employed for the synthesis of three derivatives of iron hydroxo-, fluoro-, and mixed hydroxo-fluoro phosphates LiFePO$_4$(OH)$_x$F$_{1-x}$ where 0 ≤ x ≤ 1 with the tavorite structure type, and their detail electrochemical activities have been presented. The hydrothermal synthesis of the pure hydroxo-derivative, LiFePO$_4$OH, using phosphorous acid as a source of phosphate yielded good quality crystals from which the crystal structure was solved for the first time using SC-XRD (single crystal X-ray diffraction). The fluoro derivative, LiFePO$_4$F, was prepared as a very fine powder at low temperature in a solvent-less flux-based method employing phosphorous acid and mixed alkali metal nitrates. A mixed anionic hydroxo-fluoro iron tavorite phase, LiFePO$_4$(OH)$_{0.32}$F$_{0.68}$, was also synthesized by a hydrothermal route. The electrochemical performance of the three phases was studied with galvanostatic charge–discharge tests, cyclic voltammetry, and electrochemical impedance spectroscopy (EIS). All three phases showed facile Li-insertion through the reduction of Fe^{3+} to Fe^{2+} at an average voltage in the range of 2.4–2.75 V, through the variation of the anion from pure OH to pure F. An increase of 0.35 V was observed as a result of F substitution in the OH position. Also, good cyclability and capacity retention were observed for all three phases and a reversible capacity of more than 90% was achieved for LiFePO$_4$F. The results of EIS indicated that lithium ion mobility is highest in the mixed anion.

Introduction

Polyanion-based compounds of transition metals have been actively investigated as cathode materials for Li-ion batteries since the discovery of electrochemical activity in LiFePO$_4$ by Goodenough's group.[1] The polyanions, especially phosphates, sulfates, silicates and borates are capable of forming a wide variety of 2-dimensional (2D) and 3-dimensional (3D) structures with transition metals, which are stable and amenable for facile electrochemical Li-ion insertion.[2] There are several other advantages of polyanion based materials over simple oxides. The electronegativity of the central atom of the polyanion due to its inductive effect increases the potential of the transition metal redox couple M^{n+}/M$^{(n-1)+}$ with respect to Li$^+$/Li compared to pure oxides.[3] Secondly, the polyanion-based cathodes are inherently safer due to the strong covalent bond between the central atom (P, Si, S, and B) and the oxygen, which prevents them from dissociation when the cell is fully charged or fully de-lithiated. All these characteristics have made these materials excellent candidates for motor vehicle application where safety is of utmost importance. In this regard olivine LiFePO$_4$ has been touted as an excellent candidate for hybrid electric vehicle application due to its reasonably high energy density with an average voltage of 3.5 volt *vs.* Li$^+$/Li and a theoretical capacity of 170 mA h g^{-1}.[4] However, olivine LiFePO$_4$ also suffers from limitations due to poor electronic conduction and 1-dimensional Li-ion diffusion channel.[5] To overcome this drawback, carbon coating and nano-structuring are essential to achieve near theoretical capacity at fast discharge rate, which eventually reduces the cost effectiveness of the material.[6,7] Recently, attention has been paid to another structure type namely, tavorite, with 3-D intersecting channels conducive for facile Li-ion transport.[8] The sulfate version of iron tavorite, LiFeSO$_4$F, showed excellent performance which can potentially outperform olivine LiFePO$_4$.[9] The iron tavorite phosphate phases show an average voltage of 2.6–2.8 volts for the hydroxo and fluoro derivatives, which is lower than LiFePO$_4$ and is caused by the structural differences with LiFePO$_4$.[10–15] However, iron tavorite phases can be competitive for stationary application such as in smart grid, where safety, long cycle and calendar life, environmentally friendliness and low cost of the cathode materials supersede the need of high specific energy and energy density

Department of Chemistry, Missouri University of Science and Technology, 400 W 11th Street, Rolla, MO 65409, USA. E-mail: choudhurya@mst.edu; Fax: +1-573-341-6033; Tel: +1-573-341-6332

† Electronic supplementary information (ESI) available: Details of crystal structure in the CIF format and extended CVs for each phase are available. See DOI: 10.1039/c4ra05391e

constraints of mobile applications.[16] Although tavorite iron phosphate, especially the fluoro derivative, fulfils all the above criteria, they still require an inexpensive and scalable synthesis route for large scale industrial production. High temperature ceramic methods,[12] ionothermal,[11] and solvothermal[13] routes reported so far for the synthesis of iron phosphate fluoro tavorite are cost prohibitive. In this article we report an innovative synthesis of fluoro ($LiFePO_4F$) and hydroxo ($LiFePO_4(OH)$) iron tavorite phases employing phosphorous acid as a source of phosphate in a low temperature flux and hydrothermal reactions, respectively. In addition we also report the synthesis of mixed fluoro/hydroxo phase, $LiFePO_4(OH)_{0.32}F_{0.68}$, by a hydrothermal reaction. The products were characterized by powder and single-crystal X-ray crystallography, IR and Mössbauer spectroscopic techniques and thermogravimetric analysis. Although structure of full hydroxo tavorite has been reported from powder X-ray- and neutron diffraction data,[10] the single-crystal X-ray structure determination is reported here for the first time. Finally we present a comparison of the electrochemical Li-ion activities of the three phases with respect to charge–discharge, cyclic voltammetry, and electrochemical impedance measurements.

Experimental

Materials

$LiNO_3$, KNO_3, LiOH and H_3PO_3 were purchased from Acros Organics, $Fe(NO_3)_3 \cdot 9H_2O$ from Alfa Aesar and Li foil from Sigma-aldrich. All the chemicals used without further purification.

Synthesis

$LiFePO_4F$ has been synthesized employing a low melting flux consisting of KNO_3–$LiNO_3$ eutectic mixture and phosphorous acid (H_3PO_3). In a typical synthesis 8.08 g of $Fe(NO_3)_3 \cdot 9H_2O$ (20 mmol), 0.52 g (20 mmol) of LiF, and 1.64 g (20 mmol) H_3PO_3 were added in 14 g of KNO_3–$LiNO_3$ mixture (0.56 : 0.44) in a 23 mL Teflon-lined stainless steel Parr acid digestion bomb. The Parr reactor containing the reaction mixture was placed in a 200 °C oven and heated at that temperature for 72 h, after that the bomb was removed from the oven and allowed to cool naturally. The product which consisted of white fine powder was washed with chilled water several times to remove LiF completely and then dried in air.

$LiFePO_4(OH)$ was prepared hydrothermally employing H_3PO_3 as source of phosphate. In a typical synthesis 16.16 g (40 mmol) of $Fe(NO_3)_3 \cdot 9H_2O$, 2.87 g (120 mmol) of LiOH, and 9.84 g (120 mmol) of H_3PO_3 were added in a beaker containing 40 mL of deionized water. The reaction mixture was stirred for several minutes to form a homogeneous solution. The reaction mixture was then transferred to a 120 mL capacity Teflon-lined stainless steel Parr reaction vessel. The reaction vessel was then placed in a 200 °C oven and heated at that temperature for 96 h, after that it was removed from the oven and allowed to cool naturally. This process yielded bright green color product

containing good quality crystals suitable for single-crystal X-ray structure determination.

$LiFePO_4(OH)_{0.32}F_{0.68}$ was prepared by hydrothermal method from a well homogenized reaction mixture of 1.35 g (5.0 mmol) of $FeCl_3 \cdot 6H_2O$, 1.04 g (25 mmol) of $LiOH \cdot H_2O$, 0.34 mL (5.0 mmol) H_3PO_4 (85%), 0.35 mL (10 mmol) HF (49–51%) and 9 mL of deionized water in a 23 mL Teflon-lined stainless steel Parr reaction vessel. The Parr reaction vessel was heated at 175 °C for 72 h. The product, pale green powder was filtered, washed with hot water and acetone and subsequently dried in air.

Material characterization

Single-crystal X-ray diffraction. Single-crystal X-ray diffraction studies of $LiFePO_4(OH)$: crystal structure of $LiFePO_4(OH)$ was solved from single-crystal intensity data sets collected on a Bruker Smart Apex diffractometer with monochromated Mo Kα radiation ($\lambda = 0.7107$ Å). Suitable crystal was selected and mounted on a glass fiber using epoxy-based glue. The data were collected at room temperature employing a scan of 0.3° in ω with an exposure time of 20 s per frame. The data sets were collected using SMART[17] software, the cell refinement and data reduction were carried out with SAINT,[18] while the program SADABS[18] was used for the absorption correction. The structure was solved by direct methods using SHELX-97 (ref. 19) and difference Fourier syntheses. Full-matrix least-squares refinement against $|F^2|$ was carried out using the SHELXTL-PLUS[19] suit of programs. The structure of $LiFePO_4(OH)$ was solved in $P\bar{1}$ space group. The positions of two Fe atoms, Fe1 and Fe2 were located in 1c and 1a Wyckoff positions, respectively; one P and 5 O atoms were located in 2i positions from the difference Fourier maps. These positions were then refined isotropically and immediately the position of Li (2i) clearly appeared around 2 Å away from the oxygen atoms. At this point anisotropic refinement was carried out and a q peak appeared around 1 Å away from the oxygen (O3), which was bridging the two Fe-atoms. This peak was assigned as hydrogen and refined isotropically without any constraints. After the refinement O–H bond distances changed to 0.778 Å. Details of the final refinements and the cell parameters for $LiFePO_4(OH)$ are given in Table 1. The final atomic coordinates and the isotropic displacement parameters are given in Table 2. Selected inter-atomic distances are listed in Table 3.

Powder X-ray diffraction (PXRD). Phase purity for all samples was evaluated by X-ray powder diffraction patterns obtained from a PANalytical X'Pert Pro diffractometer over a 2θ range of 5 to 90° with scanning rate of 0.0236° s^{-1}.

Mössbauer spectroscopy. [57]Fe Mössbauer experiments were performed in transmission geometry at room temperature using a conventional constant acceleration spectrometer. The data were collected using a [57]Co (50 mCi) gamma-ray source embedded in a Rh matrix. Velocity calibration and isomer shifts are given with respect to alpha-Fe foil at room temperature. The Mössbauer data was analyzed by Lorentzian line fitting using RECOIL software.[20]

Thermo-gravimetric analysis. Thermo-gravimetric analysis of the samples was done using a TA instrument Q50 TGA from

Table 1 Crystal data and structure refinement for LiFePO$_4$OH

Empirical formula	LiFePO$_4$OH	V	174.81(6) Å^3
Formula weight	174.77 g mol^{-1}	Z	2
Crystal system	Triclinic	ρ_{calc}	3.320 g cm^{-3}
Space group	$P\bar{1}$	$F(000)$	170
a	5.3506(10) Å	Temperature	293 K
b	7.2877(14) Å	GOF on F^2	1.265
b	5.1174(10) Å	R factors [$I > 2\sigma(I)$]	$R_1 = 0.0393$ w$R_2 = 0.1126$
α	109.237(2)°		
β	97.878(2)°	R factors [all data]	$R_1 = 0.0437$ w$R_2 = 0.1145$
γ	106.397(2)°		

Table 2 Atomic coordinates and equivalent isotropic displacement parameters for LiFePO$_4$OH

Atoms	x	Y	z	U (eq.)	SOF
Fe(1)	0	0.5	0	0.0064(3)	0.5
Fe(2)	0	0	0	0.0062(3)	0.5
P(1)	0.6373(3)	0.7688(2)	0.3245(3)	0.0055(3)	1
O(1)	0.6588(7)	0.8802(6)	0.1146(8)	0.0082(10)	1
O(2)	0.3397(7)	0.6626(6)	0.3103(8)	0.0086(10)	1
O(3)	0.9529(8)	0.2774(6)	0.1579(8)	0.0086(10)	1
O(4)	0.7869(8)	0.6160(6)	0.2682(8)	0.0088(10)	1
O(5)	0.2456(7)	0.0689(6)	0.3670(7)	0.0075(10)	1
Li(1)	0.613(2)	0.1826(19)	0.254 (2)	0.024(3)	1
H(1)	1.027(14)	0.326(10)	0.319(16)	0.007(16)	1

Table 3 Selected bond lengths for LiFePO$_4$OH

Bonds	Distances (Å)	Bonds	Distances (Å)
Fe1–O2	1.996(4)	Fe2–O5^c	1.959(3)
Fe1–O3^b	2.009(4)	Fe2–O3^e	2.018(4)
Fe1–O4^b	2.027(4)	Fe2–O1^f	2.042(4)
Fe1–O2^d	1.996(4)	P1–O1	1.543(4)
Fe1–O3^f	2.009(4)	P1–O2	1.541(4)
Fe1–O4^f	2.027(4)	P1–O4	1.523(5)
Fe2–O5	1.959(3)	P1–O5^g	1.538(4)
Fe2–O1^a	2.042(4)	O3–H1	0.78(8)
Fe2–O3^b	2.018(4)		

^{a} $-1 + x, -1 + y, z.$ ^{b} $-1 + x, y, z.$ ^{c} $-x, -y, -z.$ ^{d} $-x, 1 - y, -z.$ ^{e} $1 - x, -y, -z.$
^{f} $1 - x, 1 - y, -z.$ ^{g} $1 - x, 1 - y, 1 - z.$

room temperature up to 800 °C with a heating rate of 10 °C min^{-1} in N$_2$ atmosphere.

IR spectroscopy. IR spectra were obtained using a Thermo Nicholet Nexus 470 FT-IR spectrometer on KBr pellets in the wavenumber range of 400 to 4000 cm^{-1}.

SEM. The morphology of the powders was studied by scanning electron microscopy (Hitachi S570) at 10 kV with a LaB$_6$ thermionic electron gun.

Fluorine analysis. For determination of fluorine content in the mixed hydroxo-fluoro iron tavorite, LiFePO$_4$(OH)$_{1-x}$F$_x$, a dried and accurately weighed sample was digested in acid and the fluoride ion concentration was subsequently measured with fluoride ion selective electrode calibrated against different concentrations of a standard (NaF) solutions; accordingly x was found to be 0.68.

Electrochemical testing. For electrochemical studies cathode mixture was prepared by mixing the active cathode material (tavorite) with Super P conductive carbon and poly-vinylidene fluoride (PVDF) as binder in 75 : 15 : 10 weight ratio. First, the mixture of active material and carbon was ball milled in a SPEX 8000D ball mill for 1 to 2 h. PVDF was then added to this fine mixture followed by an appropriate amount of *N*-methyl-2-pyrrolidone (NMP) to dissolve the PVDF. This slurry was then further ball milled for about 15 minutes to form a uniform mixture. The resulting paste was spread into a uniform film on aluminum current collector foil manually with the help of a glass rod. The prepared composite cathode sheet was kept in vacuum oven at 90 °C for 12 h. Circular disks of 3/8 inch diameter were then cut from the composite cathode film and moved to argon filled glove box (oxygen level below 3 ppm) for cell assembly. The loading of the active cathode materials in the disk was about 4–4.5 mg.

CR2032 type coin cells were assembled with the prepared composite cathode disks as positive electrode and lithium foil (thickness 0.75 mm) as the anode. A Celgard® 2325 sheet was placed between cathode and anode to act as a separator and 1 M LiPF$_6$ dissolved in ethylene carbonate (EC) and dimethyl carbonate (DMC) solution in 1 : 1 ratio was used as an electrolyte. The whole assembly was pressed using a coin cell crimper to fabricate the cell and aged for 12 h before electrochemical charge–discharge experiments.

A PAR EG&G potentiostat/galvanostat model 283 was used for recording the CV over the range of 1.5 to 4.0 V *vs.* Li/Li$^+$ with a scan rate of 0.02 mV s^{-1}. Galvanostatic charge–discharge experiments were carried out on an Arbin Instruments battery tester model BT2043. Electrochemical impedance spectra were collected with an Ivum Stat Impedance Analyzer at 30 °C in a frequency range of 10 mHz to 100 KHz with AC signal amplitude of 5 mV and the resulting Nyquist plots were analyzed with ZView software.

Results and discussion

Synthesis, structure and morphology

The method of synthesis is very important for the application of the material as cathode in Li-ion battery. Different synthesis methods produce different morphologies, particle sizes, and crystallinities. The hydrothermal synthesis of LiFePO$_4$(OH) reported by Marx *et al.*[10] and Ellis and Nazar[14] are very similar

and yielded product with platelet morphology. On the other hand our hydrothermal synthesis reported here starting with completely different starting precursors yielded good quality single crystals. Similarly, synthesis of LiFePO$_4$F, which was so far achieved by three different methods namely ionothermal, high temperature solid-state, and solvothermal synthesis. The ionothermal synthesis of LiFePO$_4$F reported by Tarascon group,[11] involves expensive ionic liquids, has produced nanometer sized particles. A high temperature (575–750 °C) ceramic method,[12] which is not energy efficient, has produced highly crystalline phase of LiFePO$_4$F with micron sized particles often requiring extensive ball-milling to produce fine particles for electrochemical application. The solvothermal route reported by Nazar group also requires careful drying of the ethanol to produce OH free LiFePO$_4$F phase of elongated particles.[13] In this manuscript we are reporting for the first time a flux based solvent free method for the synthesis of LiFePO$_4$F starting with H$_3$PO$_3$, iron nitrate, and mixed alkali metal nitrates at relatively low temperature (200 °C). It is to be noted here that in these reactions the phosphorous acid is acting as a precursor for phosphate moiety; aided by the strong oxidizing nature of the reaction mixture due to the presence of nitrate anions in solution (in the case of LiFePO$_4$OH) or in the molten salt mixture (in the case of LiFePO$_4$F). The following redox reaction (1) appears to occur as evident by the evolution of yellow-orange NO$_2$ gas on opening the reaction vessel after completion of the reaction:

$$2NO_3^- + H_3PO_3 \rightarrow 2NO_2 + H_2O + HPO_4^{2-} \qquad (1)$$
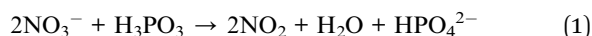
To compare the electrochemical activities of the two end members, pure hydroxo and pure fluoro, we have also synthesized a mixed anionic solid solution, LiFePO$_4$(OH)$_{0.32}$F$_{0.68}$. The hydrothermal synthesis reported is different from Ellis and Nazar[14] and produces micrometer long bar-shaped crystallites. Genkina *et al.* first reported the single-crystal structure of a synthetic tavorite of the composition LiFePO$_4$(OH, F).[21] Yakubovich on the other hand reported a single-crystal study of a tavorite related phase with an additional Fe-sites and a mixed valency of Fe with the composition LiFe^{3+}Fe$_x^{2+}$[PO$_4$][(OH)$_{1-2x}$O$_{2x}$].[22] In the former, Li-site has been described as 6-coordinate, while the latter has two partially occupied 5 coordinate Li-sites. To our knowledge there is no report of single-crystal structure solution of pure LiFePO$_4$(OH) from X-ray data. Recently, high quality X-ray and neutron powder data has been used to solve the structure of pure LiFePO$_4$(OH) phase by Marx *et al.*[10] and our single-crystal structure determination fully corroborates with that report. Both Fe1 and Fe2 adopt octahedral geometry, where Fe–O distances are in the range 1.995(3)–2.0274(4) Å and 1.958(2)–2.042(3) Å, respectively, for Fe1 and Fe2. The Li ion is surrounded by 5 oxygen atoms in an irregular polyhedron, with Li–O distances in the range 1.944(4)–2.177(5) Å. Both Fe–O and Li–O distances are in very good agreement with Marx *et al.*'s neutron solution. Fe1 and Fe2 are located on the center of inversion at (0, 0.5, 0) and (0, 0, 0), respectively, and Fe1O$_6$ and Fe2O$_6$ octahedra are connected through the corner (O3) to form a one-dimensional corner-shared chain along the *a*-lattice vector. These chains of octahedra are then cross-linked by the phosphate tetrahedra to form the three-dimensional structure.

Such connectivity also leads to channels in all the three crystallographic directions (Fig. 1). The Li-ions are located in channels along the *c*-axis; on the other hand hydrogen attached to the bridging oxygen (O3) protrudes in the channels along the *a*-axis. It is also interesting to note that anisotropic thermal parameters for Li ($U_{11} = 21$, $U_{22} = 31$, and $U_{33} = 17$ Å $\times$ 10^3) indicate more vibrations of Li along *ab*-plane compared to *c*-axis, an observation similar but less pronounced compared to the data from neutron refinement.[10]

The powder XRD patterns of two as prepared tavorite phases are shown in Fig. 2. The experimental powder patterns for LiFePO$_4$(OH) and LiFePO$_4$(OH)$_{0.32}$F$_{0.68}$ were compared with the simulated powder X-ray pattern from the single-crystal coordinates of LiFePO$_4$(OH). The excellent agreement between the simulated and the experimental patterns indicate phase purity of LiFePO$_4$(OH), however, a small amount of LiF impurity phase can be seen in the as synthesized mixed anion phase, which goes away on repeated washing with chilled water.

For the full fluoro derivative, LiFePO$_4$F, a Rietveld refinement has been performed using GSAS-II software on a high resolution PXRD data.[23] Unit cell parameters, space group ($P\bar{1}$), and atomic coordinates for the starting model were taken from Nazar group publication.[13] Unit cell parameters, fractional atomic coordinates, isotropic thermal displacement parameters, and site occupancy for lithium ion were subsequently refined. Accordingly, the occupancy of two disordered lithium sites was refined to a value of each having 50% occupancy, which is slightly different from that reported by Nazar group. The refinement was converged with $R_w = 2.11\%$ (Fig. 3) and the
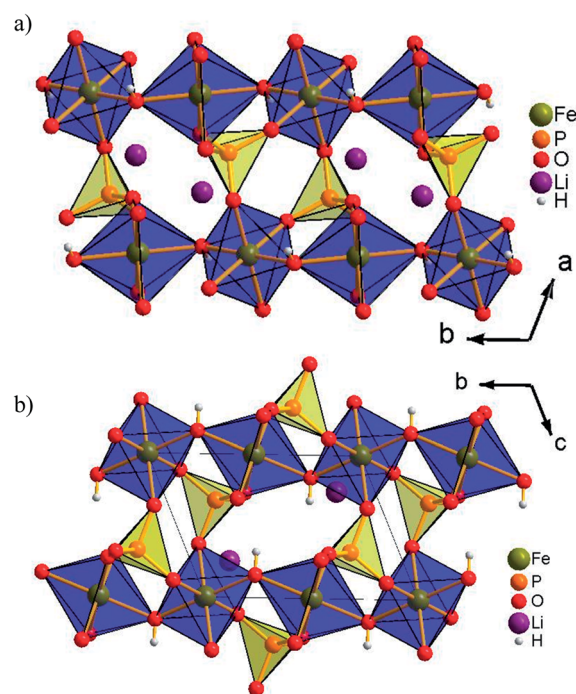

Fig. 1 Polyhedral representation of LiFePO$_4$(OH) structure with Fe1 and Fe2 at the center of blue octahedra; (a) view along the *c*-axis; (b) view along the *a*-axis.
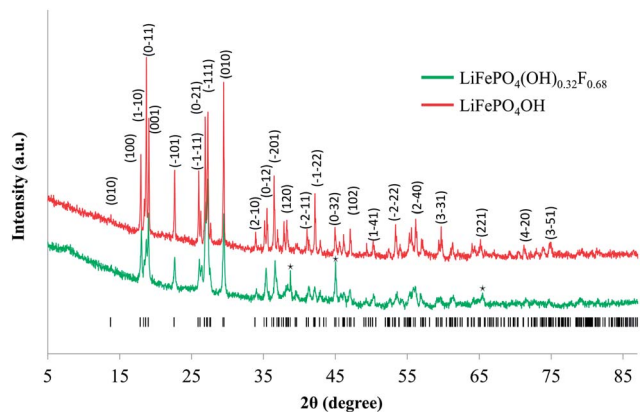
Fig. 2 Observed and calculated XRD patterns for the two prepared tavorite phases. LiF impurity phase is marked with an asterisk.

resulting cell parameters [$a = 5.296(2)$ Å, $b = 7.256(5)$ Å, $c = 5.140(3)$ Å, $\alpha = 108.43(7)°$, $\beta = 98.05(6)°$, $\gamma = 107.16(1)°$, $V = 173.05(2)$ Å^3] are in good agreement with that reported by Nazar group.[13]

Fig. 4 demonstrates the typical SEM micrographs of the samples. The SEM images reveal great differences in the morphology between the three samples. As synthesized LiFePO$_4$(OH) particles are composed of polyhedral crystals of various sizes fused together to form secondary particles, several tens of micrometers in diameter. LiFePO$_4$(OH)$_{0.32}$F$_{0.68}$ on the other hand includes strip like crystals with submicron width and thickness and the synthesis procedure for LiFePO$_4$F yields small plate-like crystals which are several hundred nanometers in thickness.

Spectroscopic and thermo-gravimetric analysis

Fig. 5 shows the FTIR spectra of the three samples with vibrational modes for phosphate in the range of 940–1160 cm^{-1}. The –OH bending and stretching modes are clearly observed at 795 and 3270 cm^{-1}, respectively, for the LiFePO$_4$OH phase. As expected the intensity of the –OH vibrational modes decreased

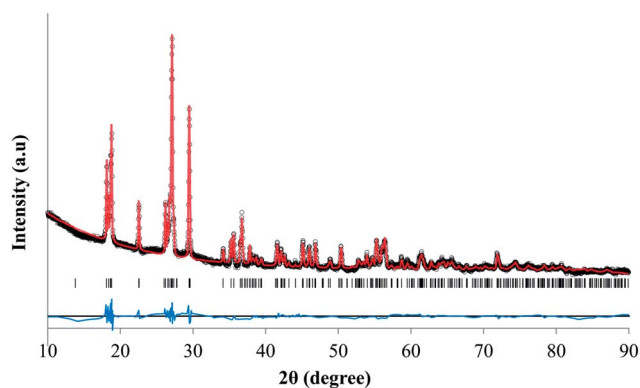Fig. 3 Calculated (red line) and experimental (open circles) curves after Rietveld refinement on XRD pattern of LiFePO$_4$F.

in LiFePO$_4$(OH)$_{0.32}$F$_{0.68}$ compared to LiFePO$_4$(OH) and disappear completely in LiFePO$_4$F.

Fig. 6 exhibits the Mössbauer spectra for the three different samples, along with the fit parameters in Table 4.

The Mössbauer spectra provide valuable information about the chemical nature of Fe in the compound. Two important parameters in Mössbauer spectrum, isomer shift (IS) and quadruple splitting (QS), are directly related to the total electron density at the Fe center which in turn gives sensitive information about valence and spin state of Fe. For each compound, the Mössbauer spectrum has been fitted with two doublets corresponding to Fe1 and Fe2. The ratio of the two doublets (1 : 1) determined from the fitting is in agreement with ratio derived from crystal structure of LiFePO$_4$(OH). The values of the isomer shift and quadruple splitting are signature of Fe in +3 oxidation state and octahedral coordination. The fitted values of IS and QS corroborates well with that reported by Delmas and Nazar groups.[10,13]

More importantly it can be seen that the isomer shift as well as quadrupole splitting between the doublets increases as the F$^-$/OH$^-$ ratio increase. This can be explained based on the reduction of the covalency of the Fe–X (X = O, F) bond with increase of fluoride anion[24,25] and that is reflected in the higher cathode potential in the case of LiFePO$_4$F (*vide infra*). Mössbauer spectra was also indicative of the fact that there was no other iron-containing impurities in any of the compounds as evident in the spectra collected over the entire velocity range spanning from −10 to +10 mm s^{-1} (data not shown). Mössbauer spectrum for LiFePO$_4$(OH)$_{0.32}$F$_{0.68}$ also supports the substitutional solid solution of F and OH in the same crystallographic site and is statistically distributed throughout the structure. If LiFePO$_4$(OH)$_{0.32}$F$_{0.68}$ was a heterogeneous mixture of 32% pure hydroxo and 68% of pure fluoro derivative or if there were fluoro or hydroxo rich regions in the structure then signature of both end member would have been found in the Mössbauer spectra.

TGA was conducted to assess the thermal stability of each compound and the results are presented in Fig. 7.

LiFePO$_4$OH decomposes at 450 °C to Li$_3$Fe$_2$(PO$_4$)$_3$, Fe$_2$O$_3$, and H$_2$O in agreement with previous results,[13] and approximately 5.15% weight loss can be accounted for by the removal of H$_2$O. LiFePO$_4$F is stable up to 550 °C, about 50 °C lower than that reported by Nazar *et al.*[14] This lower thermal stability can be assigned to smaller particle sizes of our sample. It is expected that LiFePO$_4$F would follow a similar decomposition path as LiFePO$_4$OH according to the following equation, $3LiFePO_4 = Li_3Fe_2(PO_4)_3 + FeF_3$. The sluggish mass loss from 550 to 800 °C can be accounted for by the decomposition of FeF$_3$ through a reaction with impurity moisture in the N$_2$ gas and subsequent removal of HF ($2FeF_3 + 3H_2O = Fe_2O_3 + 6HF$). LiFePO$_4(OH)_{0.32}F_{0.68}$ shows a trend in between that of the other two end members of the group with two major mass loss steps. The first mass loss occurs at 450 °C, which we speculate, is due to the loss of HF according to the following equation, $3LiFe(OH)_{0.32}F_{0.68}PO_4 = Li_3Fe_2(PO_4)_3 + 1/3FeF_3 + 1/3Fe_2O_3 + HF$. Above 530 °C the sluggish weight loss may be due to the decomposition of FeF$_3$ due to the presence of impurity moisture similar to LiFePO$_4$F.
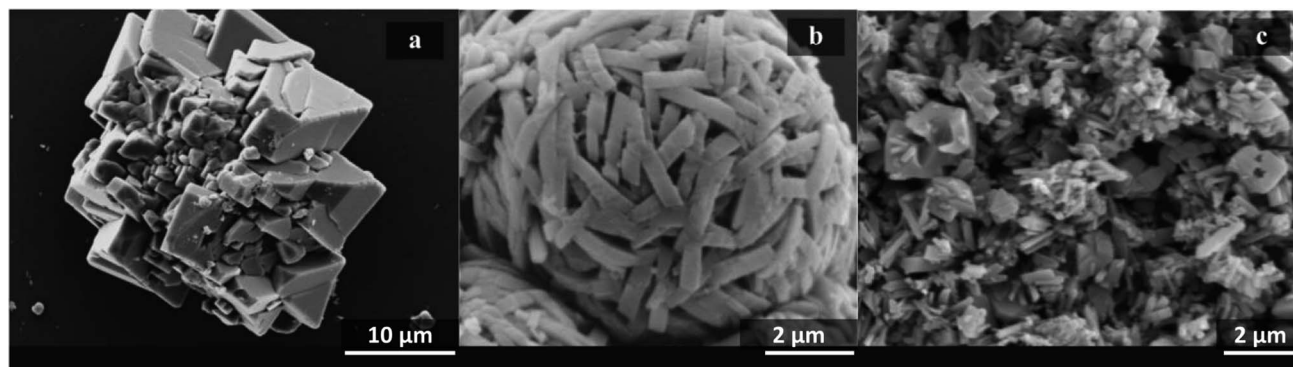
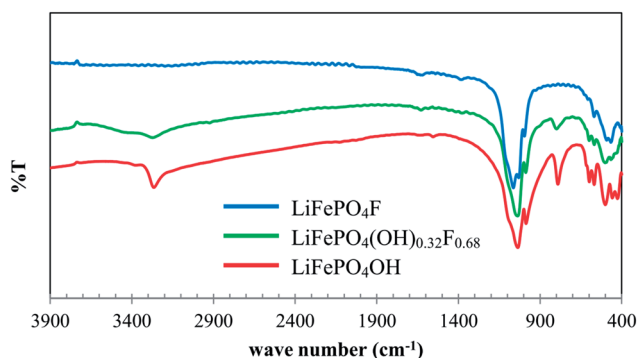Fig. 4 SEM images of $LiFePO_4OH$ (a); $LiFePO_4(OH)_{0.32}F_{0.68}$ (b) and $LiFePO_4F$ (c).

Fig. 5 FTIR spectra of the three phases of $LiFePO_4(OH)_xF_{1-x}$ where $0 \leq x \leq 1$.

Table 4 Values of fit parameters for isomer shift (δ), quadrupole splitting (ΔE) and site percentage for $LiFePO_4OH$, $LiFePO_4(OH)_{0.32}F_{0.68}$ and $LiFePO_4F$

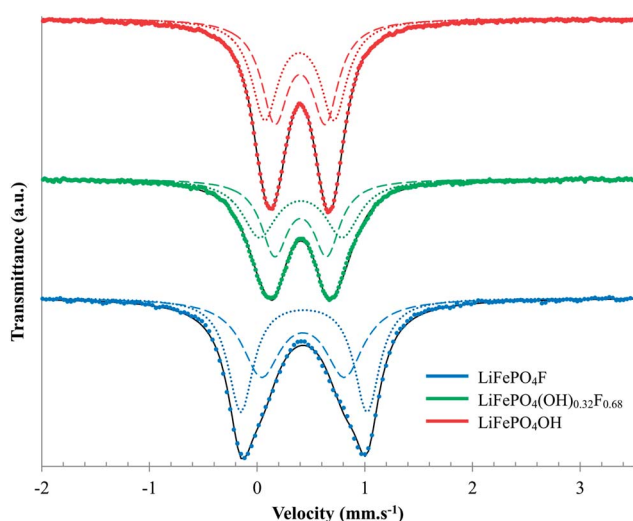|		Doublet 1	Doublet 2
$LiFePO_4OH$	δ (mm s^{-1})	0.398(9)	0.392(6)
	ΔE (mm s^{-1})	0.469(2)	0.641(1)
	%Fe	50.016(4)	49.983(6)
$LiFePO_4(OH)_{0.32}F_{0.68}$	δ (mm s^{-1})	0.404(4)	0.406(4)
	ΔE (mm s^{-1})	0.483(3)	0.769(4)
	%Fe	50.000(4)	49.999(6)
$LiFePO_4F$	δ (mm s^{-1})	0.425(8)	0.434(6)
	ΔE (mm s^{-1})	0.772(4)	1.173(1)
	%Fe	49.947(8)	50.052(2)

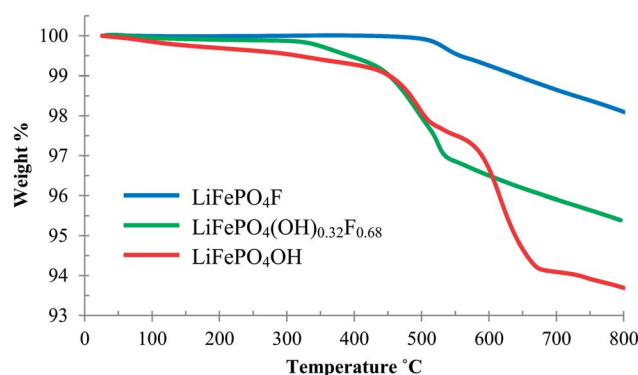Fig. 6 Mössbauer spectra of three prepared iron tavorite phases; experimental data: dots; doublets 1 and 2: dashed and dotted line; solid line: fitted curve.

Fig. 7 TGA plots of three iron tavorite phases.

The open circuit voltage (OCV) values for $LiFePO_4(OH)$, $LiFePO_4(OH)_{0.32}F_{0.68}$, and $LiFePO_4F$ are 3.05, 3.15, and 3.06 V, respectively. The cathodic (Li-insertion) and anodic (Li-extraction) peaks are observed at 2.29 and 2.59 V for $LiFePO_4(OH)$, 2.43 and 2.94 V for $LiFePO_4(OH)_{0.32}F_{0.68}$, and 2.65 and 3.19 V for $LiFePO_4F$. Besides the main anodic and cathodic peaks, $LiFePO_4(OH)$ shows an additional broad anodic peak centered at 2.78 V, which may indicate phase transformation during oxidation. On the other hand $LiFePO_4(OH)_{0.32}F_{0.68}$ shows low intensity shoulders in both anodic and cathodic peaks at higher
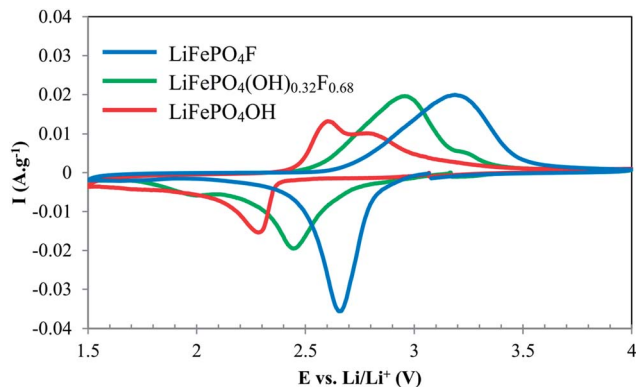
Electrochemistry

Cyclic voltammetry. Fig. 8 shows the first cycle of cyclic voltammograms of composite electrodes made from these tavorite phases.

Fig. 8 First cycle of cyclic voltammograms for the three tavorite phases at 0.02 mV s^{-1}. Cathodic current is negative.

Fig. 9 Voltage–composition profiles for the first 3 discharge curves of: $LiFePO_4OH$ (a); $LiFePO_4(OH)_{0.32}F_{0.68}$ (b) and $LiFePO_4F$ (c) at $C/50$. First discharge and charge: ▬; second discharge and charge: ▬; third discharge: ▬. Inset in each figure shows the achievable specific discharge capacity at different C-rates on consecutive cycles.

and lower voltages than the main peaks, respectively. Upon successive cycling the shoulder peaks as well as the main anodic and the cathodic peaks shift to higher and lower potentials, respectively, indicating increased electrode polarization due to cycling (ESI†). The increasing trend of discharge potential with increasing fluoride content in conjunction with the results from Mössbauer spectra suggests that incorporation of fluoride anion leads to the increased cell potential in the full fluoro tavorite version. Also notably, the area under cathodic curve is considerably larger for $LiFePO_4F$ compared to $LiFePO_4(OH)$, suggesting higher overall discharge kinetic capabilities of the former.

Galvanostatic charge–discharge. Based on the results from CVs, cutoff potentials were set at 4.0 and 1.5 V for running galvanostatic charge–discharge experiments. The voltage composition profiles for $LiFePO_4OH$, $LiFePO_4(OH)_{0.32}F_{0.68}$, and $LiFePO_4F$ are given in Fig. 9.

As can be observed, $LiFePO_4OH$ delivers a specific capacity 102 mA h g^{-1} during the first discharge at $C/50$, which is 67% of the theoretical capacity (153 mA h g^{-1}) followed by an irreversible capacity loss of about 6 mA h g^{-1} (6%) on the second cycle but stabilizes to almost constant capacity on subsequent cycles. It is to be noted here that during the 1st discharge the voltage drop was gradual from 3 volt (OCV) to 2.37 volt and then discharge curve shows a plateau at 2.32 volt till 0.45 Li insertion (69 mA h g^{-1}). However, on the subsequent cycles the discharge plateau is observed at 2.5 V. This gain of 0.13 V in the discharge voltage has also been observed by Nazar group[13] and has been attributed to the fact that reductive Li-insertion into $LiFePO_4OH$ leads to an amorphous phase of Li_2FePO_4OH, which remains amorphous upon oxidation. Therefore, subsequent discharge–charge cycles take place from an amorphous phase and results in an increase of discharge voltage. For assessing the cell capacity retention, it has been subjected to multiple charge–discharge cycles at higher C-rates. The results given in inset of Fig. 9a demonstrate that essentially there is a loss of capacity at higher C-rate due to electrode polarization. However, upon slowing down the C-rate, the initial capacity can be fully recovered at 96 mA h g^{-1} at $C/50$. This suggests that the capacity loss due to fast C-rate was limited by the kinetics of Li-diffusion
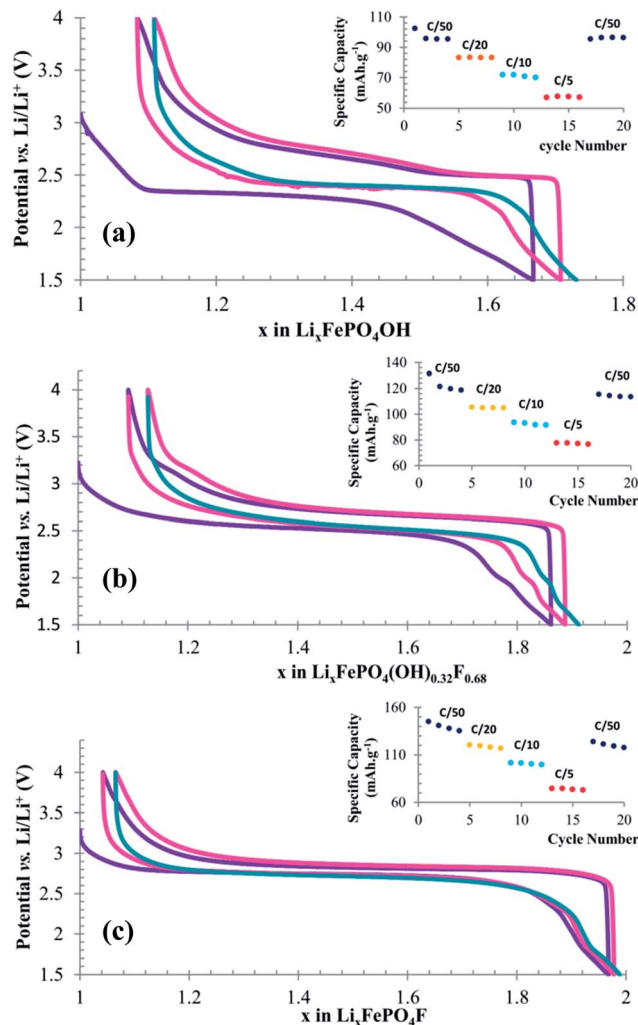
and electron transfer through the poorly conducting tavorite material and not due to any cathode degradation. On the other hand, for $LiFePO_4(OH)_{0.32}F_{0.68}$ and $LiFePO_4F$ the discharge–charge behavior is different. These two phases demonstrate good specific capacity achievement for the first cycle at 131 (74% of theoretical capacity) and 146 mA h g^{-1} (97% of theoretical capacity), respectively, at $C/50$ followed by an irreversible capacity fading of 10 mA h g^{-1} for $LiFePO_4(OH)_{0.32}F_{0.68}$ and 4 mA h g^{-1} for $LiFePO_4F$ in the second cycle. The difference in achievable specific capacity for the three phases may be due to the different particle sizes as can be seen from SEM images. During the first discharge for $LiFePO_4F$ the voltage gradually drops from 3.2 (OCV) to 2.90 volt which accounts for 0.1 Li insertion and then the discharge curve shows a flat plateau at 2.65 volt up to 0.7 Li insertion. After this point the voltage gradually drops to the lower cutoff point (1.5 volt). However, earlier report from Nazar group on $LiFePO_4F$ prepared by ceramic method has shown solid solution type sloping

discharge curve up to 0.4 Li insertion.[12] Although a good initial specific capacity was observed for LiFePO$_4$F, it undergoes some irreversible capacity losses as a result of cycling at different fast C-rates (inset of Fig. 9c). At 20th cycle the capacity reduces to a value of 118 mA h g^{-1} when discharge is repeated again at the initial rate of C/50. On the contrary, LiFePO$_4$(OH)$_{0.32}$F$_{0.68}$ exhibit a gradual sloping profile in the entire discharge–charge curve, which may indicate solid-solution type behavior during the discharge and charging. Again this discharge slope is not as steep as it was reported for LiFePO$_4$(OH)$_{0.4}$F$_{0.6}$,[14] which may be due to higher fluoride content in the current one. Capacity fading has been observed when cycled at different fast C-rates, however, the overall irreversible capacity loss after 20 cycles of charge–discharges at various C-rates is less than 8 mA h g^{-1} when the discharge is repeated again at the initial rate of C/50 (inset Fig. 9b). More importantly the capacity appears to decrease upon cycling only slightly in the case of LiFePO$_4$(OH)$_{0.32}$F$_{0.68}$.

The derivative voltage–composition curves for the three phases are shown in Fig. 10.

LiFePO$_4$OH shows two distinct phenomena close to 2.4 V during the discharge and sharp peak at 2.5 V due to the plateau arising from two phase behavior and broad peak centered around 2.6 V due to sloping charging curve. On the other hand LiFePO$_4$F demonstrate rather sharp peaks in the derivative plot, indicative of two-phase lithium insertion reactions. For LiFePO$_4$(OH)$_{0.32}$F$_{0.68}$, the case is made complicated by the fact that insertion and extraction curves are broadened considerably and there is potential overlap of reduction and oxidation peaks indicating a solid-solution type behavior during Li-insertion and extraction.

The effect of polarization (η) for the three phases as a function of C-rate is presented in Fig. 11.

LiFePO$_4$F shows the least polarization in C/50 rate, however, as the C-rate increases polarization increases abruptly suggesting the slow kinetics of lithium ion transfer in this phase. However, LiFePO$_4$(OH)$_{0.32}$F$_{0.68}$ exhibit least polarization followed by LiFePO$_4$OH and both exhibit similar sluggish increase in polarization with increasing C-rates. The relationship
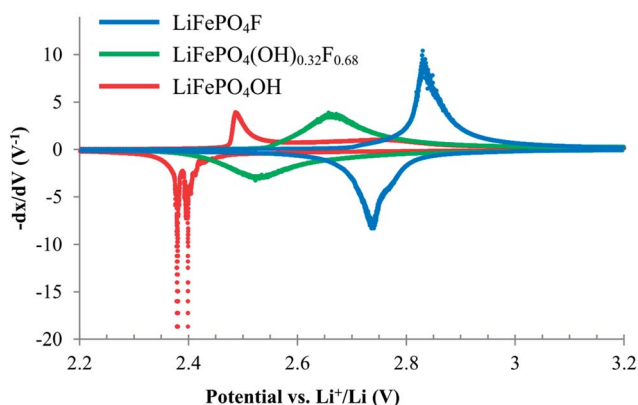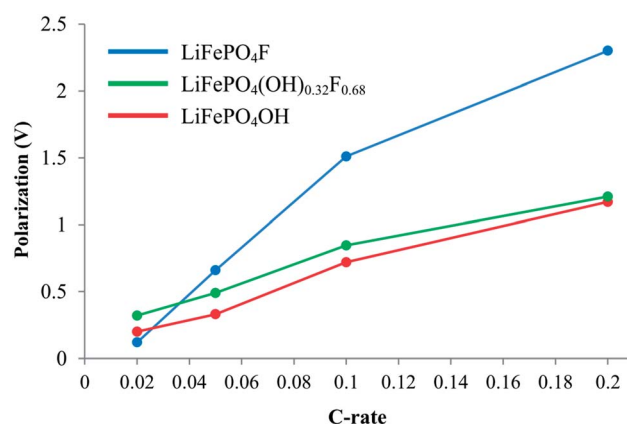

Fig. 11 Polarization as a function of C-rate for the three phases. Polarization was measured from voltage–composition curves as the separation between charge and discharge plateaus at their flattest point.

between polarization (defined as $E–E_{OCV}$) and current density (J) treated according to porous electrode theory can be approximated as:[26]

$$J \propto Fk \left[x \exp\left(\frac{\alpha_A F}{RT} (E - E_{OCV}) \right) - (1 - x)\exp \right.$$
$$\left. \times \left(-\frac{\alpha_C F}{RT} (E - E_{OCV}) \right) \right] \quad (2)$$

where F is the Faraday constant, k is the adjusted electrochemical reaction rate constant, α_A and α_C are the respective transfer coefficients for cathodic and anodic reactions on the working electrode, and x is the fraction of lithiation. Furthermore, according to the Fick's first law of diffusion:

Fig. 10 Derivatives of voltage–composition curves for the three tavorite phases.

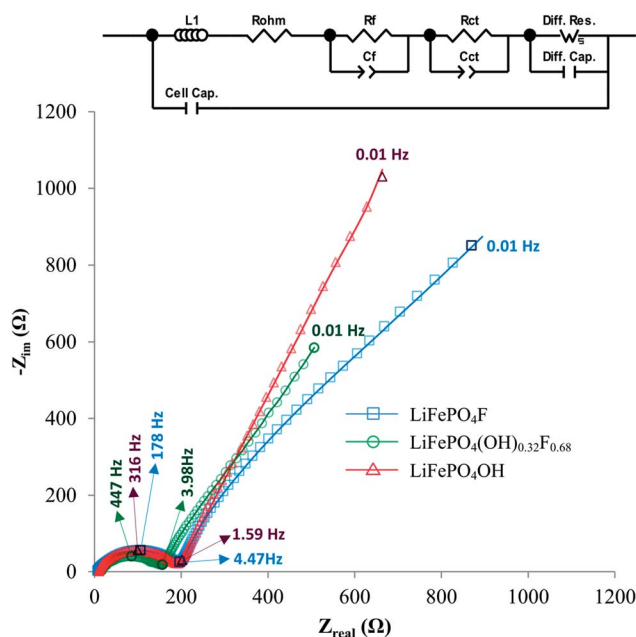**Fig. 12** Nyquist plot for LiFePO$_4$OH, LiFePO$_4$(OH)$_{0.32}$F$_{0.68}$ and LiFePO$_4$F cells with solid lines representing the fitted curve; inset: equivalent circuit model used for fitting.

Table 5 Impedance equivalent circuit fit parameters for LiFePO4OH, LiFePO4(OH)$_{0.32}$F$_{0.68}$ and LiFePO4F cells

| | L_1 (μH) | R_{ohm} (Ω) | R_f (Ω) | R_{ct} (Ω) | C_f (μF) | C_{ct} (μF) | Warburg Short^a | | | Diff. cap. (mF) | Cell cap. (nF) |
							R_w (Ω)	τ (s)	P		
LiFePO$_4$OH	4.5	9.7	83.9	98.2	12.5	89.5	7719	215	0.72	0.20	27.2
LiFePO$_4$(OH)$_{0.32}$F$_{0.68}$	3.6	9.1	53.2	99.9	2.93	20.9	2565	134	0.54	3.11	19.9
LiFePO$_4$F	2.6	5.8	199.6		56.8		4404	211	0.46	2.93	31.6

^{a} $Z_{ws} = \dfrac{R_W \times \tanh(j\omega\tau)^P}{(j\omega\tau)^P}$ where $\tau = L^2/D$ and L and D are effective diffusion length and diffusion coefficients, respectively.

$$J = -zFD(\nabla c) \qquad (3)$$

where z is the number of charges per charge carrier ($z = 1$ for lithium ion) and ∇c is the concentration gradient across the cathode solid particle. Inspection of (2) and (3) suggests that η should have an inverse logarithmic relationship with diffusivity and concentration gradient of the lithium ion in the cathode, and should not depend on particle size, as can be seen in the work of Kang et al.[27] Therefore, the higher polarization of LiFePO$_4$F compared to LiFePO$_4$(OH) or LiFePO$_4$(OH)$_{0.32}$F$_{0.68}$ at higher C-rate can be attributed to the difference in lithium ion diffusion coefficients although the particle sizes are larger for LiFePO$_4$OH and smaller for LiFePO$_4$F.

Electroimpedance spectroscopy. Electroimpedance spectroscopy (EIS) was used for further studying the lithium ion mobility in the three cathode materials and the results of experimental data and fitted curves using a general lithium-ion battery equivalent circuit model are shown in Fig. 12.[28]

In the case of LiFePO$_4$OH and LiFePO$_4$(OH)$_{0.32}$F$_{0.68}$ two parallel R|CPE elements are required to describe the medium to high frequency region which are usually assigned to solid-electrolyte interface (SEI) film and charge-transfer resistances while for LiFePO$_4$F the above two processes have very close time constant so that they are merged together and only one parallel R|CPE is sufficient for modeling. Note that the low frequency tail of the impedance spectra in all cases is characteristic of the ionic nature of conductivity. Interestingly, of the three derivatives LiFePO$_4$(OH)$_{0.32}$F$_{0.68}$ phase exhibits the highest lithium ion mobility and smallest combined charge transfer and film resistance, consistent with polarization studies mentioned above. However, low frequency part of the spectra for LiFePO$_4$F and LiFePO$_4$OH has comparable absolute impedance magnitudes. The reason for comparable absolute impedances for LiFePO$_4$OH and LiFePO$_4$F at lowest frequencies is that although LiFePO$_4$OH exhibits a higher lithium ion diffusion coefficient, it has a higher average particle size as well and the corresponding relaxation time (τ) defined as:

$$\tau = \frac{L^2}{D} \qquad (4)$$

where L is the diffusion length and D is the diffusion coefficient, becomes comparable to that of LiFePO$_4$F.

The values of fit parameters for the two systems are given in Table 5. The combined value for $R_{ct} + R_f$ and their related

capacitance obtained for LiFePO$_4$F are consistent with those reported by Prabu et al.[15]

Conclusions

Novel synthesis routes presented in this work could be used to expand the inventory of available methods for production of the iron tavorite family of materials. The crystal structure found from single crystal X-ray diffraction confirmed the accepted models which were previously based mainly on powder diffraction techniques. Moreover, the low temperature, solvent free phosphorous acid based synthesis route proposes an economical and scalable way for mass production of LiFePO$_4$F as a cheap cathode material for lithium ion batteries. The results of electrochemical tests indicate the importance of the anion on cell performance; coordination of F$^-$ anion increases the cell potential relative to OH$^-$ anion by inductive effects. Both full fluoro and full hydroxo tavorite show a two phase behavior while the mixed anionic LiFePO$_4$(OH)$_{0.32}$F$_{0.68}$ shows a solid solution like behavior during the Li-insertion and extraction. On the other hand, in terms of charge and discharge dynamics the mixed anion phase exhibited the highest lithium ion mobility.

Acknowledgements

Notes and references

1 A. K. Padhi, K. S. Nanjundaswamy and J. B. Goodenough, *J. Electrochem. Soc.*, 1997, **144**, 1188–1194.
2 C. Masquelier and L. Croguennec, *Chem. Rev.*, 2013, **113**, 6552–6591.
3 A. K. Padhi, V. Manivannan and J. B. Goodenough, *J. Electrochem. Soc.*, 1998, **145**, 1518–1520.
4 B. Dunn, H. Kamath and J.-M. Tarascon, *Science*, 2011, **334**, 928–935.
5 R. Amin, J. Maier, P. Balaya, D. P. Chen and C. T. Lin, *Solid State Ionics*, 2008, **179**, 1683–1687.

6 H. Huang, S.-C. Yin and L. F. Nazar, *Electrochem. Solid-State Lett.*, 2001, **4**, A170–A172.

7 C. Delacourt, P. Poizot, S. Levasseur and C. Masquelier, *Electrochem. Solid-State Lett.*, 2006, **9**, A352–A355.

8 J. Barker, M. Y. Saidi and J. L. Swoyer, *J. Electrochem. Soc.*, 2003, **150**, A1394–A1398.

9 N. Recham, J.-N. Chotard, L. Dupont, C. Delacourt, W. Walker, M. Armand and J.-M. Tarascon, *Nat. Mater.*, 2010, **9**, 68–74.

10 N. Marx, L. Croguennec, D. Carlier, A. Wattiaux, F. Le Cras, E. Suard and C. Delmas, *Dalton Trans.*, 2010, 5108–5116.

11 N. Recham, J.-N. Chotard, J.-C. Jumas, L. Laffont, M. Armand and J.-M. Tarascon, *Chem. Mater.*, 2010, **22**, 1142–1148.

12 T. N. Ramesh, K. T. Lee, B. L. Ellis and L. F. Nazar, *Electrochem. Solid-State Lett.*, 2010, **13**, A43–A47.

13 B. L. Ellis, T. N. Ramesh, W. N. Rowan-Weetaluktuk, D. H. Ryan and L. F. Nazar, *J. Mater. Chem.*, 2012, **22**, 4759–4766.

14 B. L. Ellis and L. F. Nazar, *Chem. Mater.*, 2012, **24**, 966–968.

15 M. Prabu, M. V. Reddy, S. Selvasekarapandian, G. V. Subba Rao and B. V. R. Chowdari, *Electrochim. Acta*, 2012, **85**, 572–578.

16 Z. Yang, J. Zhang, M. C. W. Kintner-Meyer, X. Lu, D. Choi, J. P. Lemmon and J. Liu, *Chem. Rev.*, 2011, **111**, 3577–3613.

17 Bruker, *SMART*, Bruker AXS Inc., Madison, Wisconsin, USA, 2002.

18 Bruker, *SAINT and SADABS*, Bruker AXS Inc., Madison, Wisconsin, USA, 2008.

19 G. M. Sheldrick, *Acta Crystallogr., Sect. A: Found. Crystallogr.*, 2008, **64**, 112–122.

20 K. Lagarec and D. G. Rancourt, *Nucl. Instrum. Methods Phys. Res., Sect. B*, 1997, **129**, 266–280.

21 E. A. Genkina, Y. K. Kabalov, B. A. Maksimov and O. K. Mel'Nikov, *Crystallography*, 1984, **29**, 50–55.

22 O. V. Yakubovich and V. S. Urusov, *Geochem. Int.*, 1997, **35**(7), 630–638.

23 B. H. Toby and R. B. Von Dreele, *J. Appl. Crystallogr.*, 2013, **46**, 544–549.

24 F. Menil, *J. Phys. Chem. Solids*, 1985, **46**, 763–789.

25 F. Neese, *Inorg. Chim. Acta*, 2002, **337**, 181–192.

26 M. Doyle, T. F. Fuller and J. Newman, *J. Electrochem. Soc.*, 1993, **140**, 1526–1533.

27 J. Dou, X. Kang, T. Wumaier, N. Hua, Y. Han and G. Xu, *J. Solid State Electrochem.*, 2012, **16**, 1925–1931.

28 D. Andre, M. Meiler, K. Steiner, H. Walz, T. Soczka-Guth and D. U. Sauer, *J. Power Sources*, 2011, **196**, 5349–5356.